Flexible, Transparent, and Bifacial Perovskite Solar Cells and Modules Using the Wide-Band Gap FAPbBr 3 Perovskite Absorber

Farshad Jafarzadeh, Luigi Angelo Castriotta, Marie Legrand, Daniel Ory, Stefania Cacovich, Zeynab Skafi, Jessica Barichello, Francesca de Rossi, Francesco Di Giacomo, Aldo Di Carlo, et al.

Flexible, Transparent, and Bifacial Perovskite Solar Cells Using Wide-bandgap $FAPbBr_3$ Perovskite Absorber

Farshad Jafarzadeh[a], Jessica Barichello[a], Luigi Angelo Castriotta[a], Marie Legrand [b], Daniel Ory[c], Stefania Cacovich[b], Zeynab Skafi[a], Francesca De Rossi[a], Francesco Di Giacomo[a], Aldo Di Carlo[a,d], Thomas Brown[a], Francesca Brunetti[a], Fabio Matteocci[a,*]

a CHOSE (Centre for Hybrid and Organic Solar Energy), Department of Electronic Engineering, University of Rome Tor Vergata, Via del Politecnico 1, 00133 Rome, Italy

b Institut Photovoltaïque d'Ile-de-France (IPVF), UMR 9006, CNRS, Ecole Polytechnique, IP Paris, Chimie Paristech, PSL, 91120 Palaiseau, France

c Électricité de France (EDF), R&D, 18 Boulevard Thomas Gobert, Palaiseau, 91120, France

d CNR-ISM Istituto di Struttura della Materia, via del Fosso del Cavaliere 100, 00133 Rome, Italy

* Corresponding Author

Abstract

Perovskite solar cells (PSCs) offer impressive performance and flexibility thanks to their simple, low-temperature deposition methods. Their bandgap tunability allows for a wide range of applications, transitioning from opaque to transparent devices. We present the first demonstration of flexible, bifacial PSCs using the wide bandgap $FAPbBr_3$ perovskite. The role of optimization for both electron and hole transport layers on bifaciality, transparency, and stability have been studied. PSCs achieved a maximum power conversion efficiency (PCE) of 6.8% and 18.7% under 1-Sun and under indoor light conditions, respectively, showing up to 98% bifaciality factor and an average visible transmittance (AVT) of 55%. Additionally, P1-P2-P3 laser ablation scheme has been developed on flexible PET substrate for perovskite solar modules showing PCE of 4.7% PCE and high geometrical fill factor (97.8%). These findings highlight the potential of flexible, bifacial PSCs for diverse applications like building-integrated PV, agrivoltaics, automotive tech, wearable sensors and IoT, and more.

TOC Graphic

With growing global energy demand, it is necessary to move from fossil fuels to renewable energy resources. Solar energy is a promising solution and photovoltaics technology has made significant progress in recent years. Perovskite solar cells (PSCs) have achieved impressive power conversion efficiencies (PCEs) of up to 26% in a short timeframe[1,2]. PSCs are ideal for flexible photovoltaics, as they can be deposited using simple and low-temperature solution processing methods [3–6]. Another notable characteristic of PSCs is their remarkable band-gap tunability, which can be achieved through composition engineering[7,8]. The incorporation of bromide and chloride into the perovskite composition allows for the creation of highly transparent perovskites with band gaps as high as 2.39 eV[8]. Furthermore, PSCs exhibit excellent performance in the blue-light region, making them well suited as light harvesters for diffused sunlight on cloudy days and low-intensity indoor lighting during nights [9–11]. This, combined with flexibility provide an easy installation option to seamlessly integrate PVs into surfaces such as building facades, windows and walls, sensors, electric vehicles, wearable devices, and smart displays and act as replacements for conventional energy sources[7,9,12–15].

Unlike opaque photovoltaics, ST-PVs aim to maximize both average visible transmittance (AVT) and PCE simultaneously, considering the trade-off between AVT and PCE. [14,16,17]. Consequently, a new metric, called Light Utilization Efficiency (LUE), has emerged, which represents the product of PCE and AVT[14]. LUE quantifies the potential of emergent ST-PV technologies in converting incoming visible light into electricity while maintaining rather high AVT. A suitable for applications such as smart windows, low-power displays, and automotive industry ST-PV technology should guarantee AVT greater than 50-80% [14]. The optimal bandgap range to achieve AVT values of 50-80% is typically between 2.18 and 2.32 eV [9]. Formamidinium lead bromide ($FAPbBr_3$) perovskite, which has a band gap of 2.23 eV, falls well within the optimal band gap range for achieving high AVT, and has already demonstrated AVT values exceeding 50%[18,19]. The PCE of opaque $FAPbBr_3$ solar cells typically reaches around 10%[20–22]. However, when using semitransparent back contact, PCE decreased to approximately 8%[18,19,23]. This reduction in efficiency is primarily attributed to the lack of back-reflection of the metallic back contact, which results in the reduced collection of backscattered light for harvesting. Furthermore, semitransparent solar cells often employ a thinner absorber layer to enhance the AVT of the cell. $FAPbBr_3$-based semitransparent PSCs exhibit minimal angular dependence of PCE, making them highly attractive for window-integrated applications[19]. When deposited on flexible substrates, these cells also experience a decrease in PCE, with the highest reported PCE of 5.0% for flexible opaque cells[24] and no flexible semitransparent PSCs (ST-PSCs) reported using this perovskite to the best of our knowledge. In this study, we fabricated flexible, bifacial PSCs using $FAPbBr_3$ perovskite as absorber. The devices have architecture of PET/ITO/SnO_2/$FAPbBr_3$/HTL/ITO (**Figure 1a**). First, we examined the impact of potassium (K) treatment on the SnO_2 used as electron transport layer (ETL). Secondly, we studied the effect of hole transport layer (HTL) on the device bifaciality factor and long-term stability. Lastly, we fabricated flexible, bifacial perovskite solar modules for the first time with high geometrical fill factor of 97.8%. The fabricated flex-ST-PSCs demonstrated high bifaciality factor achieving similar PCEs from both sides.

For SnO_2-based PSCs, treatment with potassium ionic salts has become a very common passivation method to improve device performance[25–28]. The cations and/or anions of these salts play various roles in increasing the performance of PSCs. For example, they can passivate defects in SnO_2 or perovskite layer, as well as act as preferred nuclei for perovskite formation by forming ionic bonds with perovskite precursors[25]. We performed potassium treatment to investigate its effectiveness in wide-bandgap bromide-based perovskite, $FAPbBr_3$, using potassium chloride (KCl) salt. **Figure 1b** presents the statistical

analysis of the J-V parameters of the flex-ST-PSC devices, while **Table 1** provides a summary of these parameters. The data is based on 20 cells fabricated for each group. The devices treated with KCl delivered a higher J_{SC} and fill factor, leading to an overall enhancement in performance. **Figure 1c** shows scanning electron microscope (SEM) images of $FAPbBr_3$ perovskite deposited on PET/ITO/SnO_2 without treatment and with KCl treatment. The average grain size of the perovskite layer is observed to increase from 550 nm for the control to 850 nm with the application of KCl treatment.

To gain better understanding of charge transportation and recombination process, we performed transient photovoltage (TPV) and transient photocurrent (TPC) measurements for control and KCl treated cells (**Figure S1**). **Figure 2d** illustrates the exponential voltage decay of cells measured at a light intensity equivalent to 1-sun. Being carried under V_{OC} condition, TPV decay only corresponds to recombination of accumulated charge carriers at the perovskite/charge transport films interface[29]. The charge carrier lifetime can be determined from the TPV data by fitting a single exponential decay equation ($\tau = \tau_0 e^{-\beta V_{OC}}$) where τ and β represent carrier lifetime and the constant decay, respectively[30–32]. The KCl treated cell showed longer decay resulting from less recombination at the perovskite/ETL surface. TPC measurement, on the other hand, represents charge carrier extraction at the transport layers since it is conducted under J_{SC} condition[29,33]. In this case faster TPC decay of KCl treated cells showcases higher charge extraction ability (**Figure S1 and Table S1**). The relation between charge carrier density and charge carrier lifetime in different light intensities, which is measured by TPV and TPC data, is illustrated in **Figure 1e**. As expected, carrier lifetime is increased when charge carrier density is reduced[30]. It is evident from the corresponding figure that these two parameters are increased for K-treated solar cells. The findings confirm the positive impact of KCl salt, not only in passivating defects in SnO_2, but also in enhancing the grain size of the perovskite layer. Therefore, potassium treatment with KCl can be identified as an effective ETL/perovskite interface passivator for $FAPbBr_3$-based devices. We included KCl treatment in the deposition procedure of cells for the following sections.

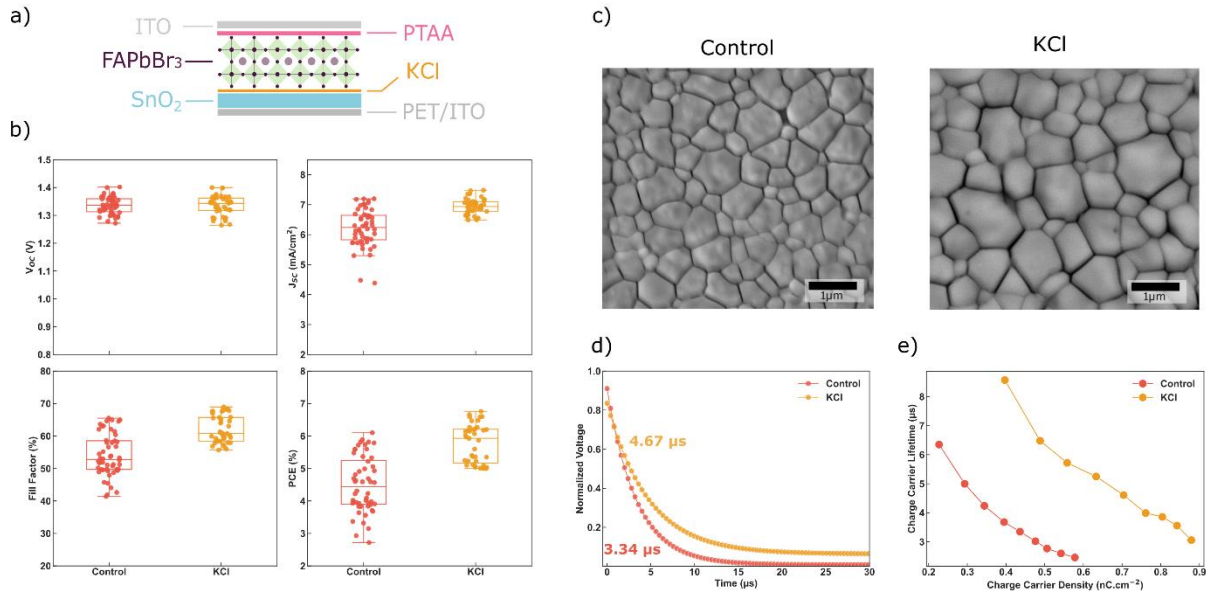

Figure 1. a. The schematic of flex-PSC cell architecture. b. Box plots depicting minimum, first quartile, median, third quartile, and maximum photovoltaic parameters of the corresponding devices based on 20 devices fabricated for control and potassium treated PSCs measured at AM1.5G illumination condition under forward and reverse scan directions. c. Scanning electron microscopy images of the $FAPbBr_3$ perovskite film deposited on top of PET/ITO/SnO_2 (control) and PET/ITO/SnO_2/KCl (KCl). d. normalized transient photovoltage decay LED light with power density of 100 mW.cm-2e. Carrier lifetime versus carrier density of solar cells.

Table 1. Summary of PV parameters of potassium treatment experiment.

Type		V_{OC} (V)	J_{SC} (mA.cm^{-2})	FF (%)	PCE (%)
Control	Best Cell	1.39	7.13	62.07	6.10
	Mean± std	1.34± 0.06	6.23± 0.91	55.05± 6.93	4.62± 0.97
KCl	Best Cell	1.40	7.35	65.70	6.8
	Mean± std	1.34± 0.04	6.94± 0.25	62.12± 4.19	5.77± 0.59

Bifacial solar cells can be illuminated from both sides. The choice of HTL choice is essential in PSCs, as the alignment of the band structures between the HTL and the perovskite layer plays a critical role in determining the V_{OC} and performance of PSCs[34,35]. However, in the case of bifacial solar cells with n-i-p architecture, the choice of HTL becomes even more crucial, particularly when bifaciality is claimed as potential way to increase the power generation thanks to albedo reflections[36,37]. In the case of bifacial operation mode, the parasitic absorption HTL can compromise the light harvesting of the perovskite absorber when the ST-PSC is illuminated from the ITO back-contact. Furthermore, the sputtering process used to deposit ITO can potentially cause damage to the HTL, leading to a decrease in overall device performance[38]. To gain a deeper understanding of $FAPbBr_3$-based flex ST-PSCs, a comparative analysis was performed on two different HTLs: PTAA and Poly-TPD (PTPD).

Figure 2 illustrates the JV curves of the champion devices under AM1.5G and indoor conditions as well as the external quantum efficiency for both HTLs when illuminated from the front and back contacts. The bifaciality factor, defined as the ratio of integrated J_{SC} obtained from the EQE measurement of cells when illuminated from the front and back, was determined to be 96% for PTAA and 98% for PTPD. PTPD outperforms PTAA with the bifaciality factor approaching unity (Integrated J_{SC} of 6.90 mA.cm^{-2} from front versus 7.01 mA.cm^{-2} from back).

PSCs offer a distinct advantage in their ability to efficiently harness light in indoor and low-light conditions[39,40]. Given that the indoor light spectrum mainly consists of blue light, perovskite solar cells demonstrate improved power conversion efficiency (PCE) under these conditions[41]. We measured cells under indoor conditions from both sides (See **Table S3**). The best indoor efficiency obtained by the PTAA-based device with 18.7% front-illuminated PCE and 17.83% back-illuminated PCE. The capability of being bifacial and flexible indoor PSCs opens up various potential low-light applications including smart home sensors, architectural integration, indoor agrivoltaics, wearable devices, and internet of things (IoT).

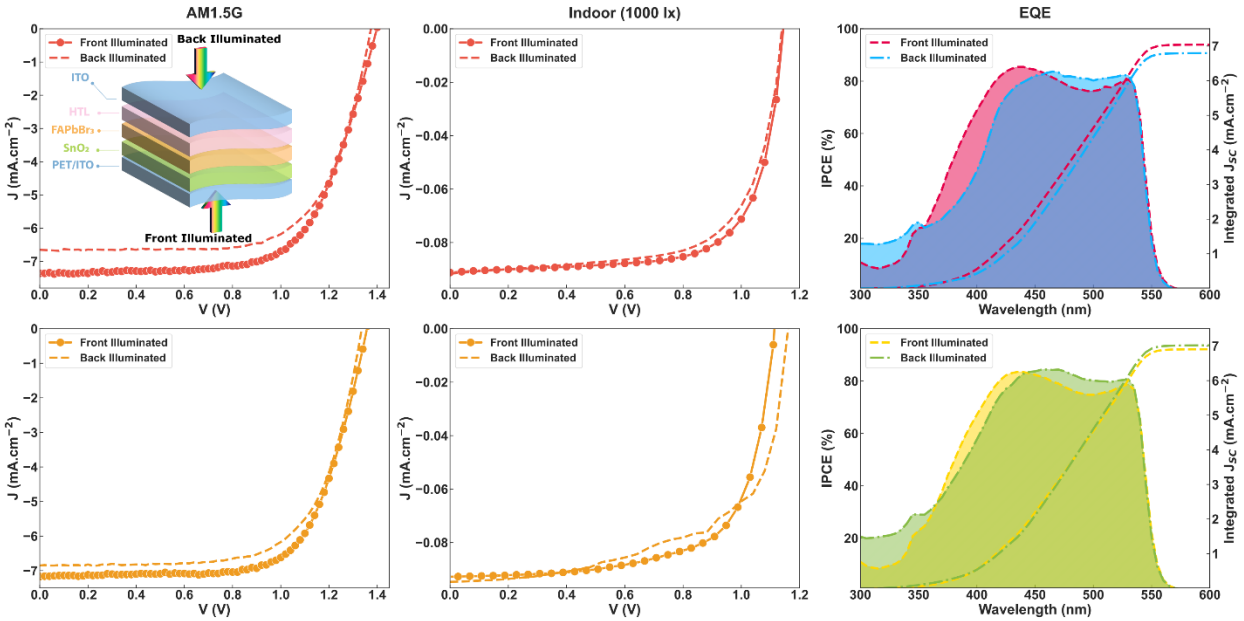

Figure 2. Bifacialty of solar cells. JV curves under AM1.5G and indoor conditions, and EQE of bifacial Flex-PSCs illuminated from front and back.

To gain deeper insights into the role played by the HTL, particularly in investigating non-radiative recombination at the absorber/HTL interface, we conducted a comprehensive analysis using absolutely calibrated photoluminescence imaging[42,43]. Specifically, three distinct stacks were examined: PET/SnO2/KCl/Perovskite, PET/SnO2/KCl/Perovskite/PTPD, and PET/SnO2/KCl/Perovskite/PTAA. In **Figure 3a-c**, we present maps of the quasi-Fermi level splitting (QFLS), derived by locally fitting hyperspectral images of photoluminescence spectra emitted under 1 sun equivalent illumination using a blue LED (405nm). An absorptivity model, corresponding to an ideal root squared absorptivity convolved with sub-bandgap tail states, was employed, as established in the formalism developed by Katahara and Hillhouse[37] whose use was already reported in previous works [42,44]. The reference sample exhibited a QFLS of 1.83 eV, while the incorporation of a transport layer led to the emergence of non-radiative recombination, resulting in a decrease of this parameter to 1.81 eV and 1.78 eV for PTPD and PTAA, respectively. These values align with those recently reported for transparent high-bandgap perovskite solar cells[23]. Notably, the samples exhibited a high level of homogeneity, with standard deviations on the order of 0.003 eV or less for the perovskite sample. The average photoluminescence spectra, depicted in **Figure 3d** reveals a gradual decrease in absolute intensity after the addition of the HTL. Additionally, a slight blue shift in the photoluminescence maximum position is observed, potentially induced by the presence of organic passivation cations derived from chloride salts added at the interface[23]. **Figure 3e** presents a comparison of optical data acquired on stacks and electrical data acquired on full devices. Radiative quasi-Fermi level splitting ($\Delta\mu_{rad}$) and radiative open circuit voltage (V_{ocrad}) are reported as theoretical limits for optical measurements and upper limits for open-circuit voltage measured by electrical means. Further details on their definitions are provided in the SI. Concerning the optical measurements, the difference between the radiative limit and the measured samples is 120 meV for the half cell, increasing to 140 meV and 160 meV for PTPD and PTAA, respectively, indicating an increase of non-radiative losses[45]. Notably, the Voc of PTAA devices is higher compared to their PTPD counterparts, a behaviour attributed to potentially more

aggressive ITO sputtering in the case of PTPD. Optimizing this final step by adding protective interlayers at the PTPD/ITO interface may allow for the full exploitation of the potential of such HTL, which has demonstrated promising characteristics according to the optical analysis results.

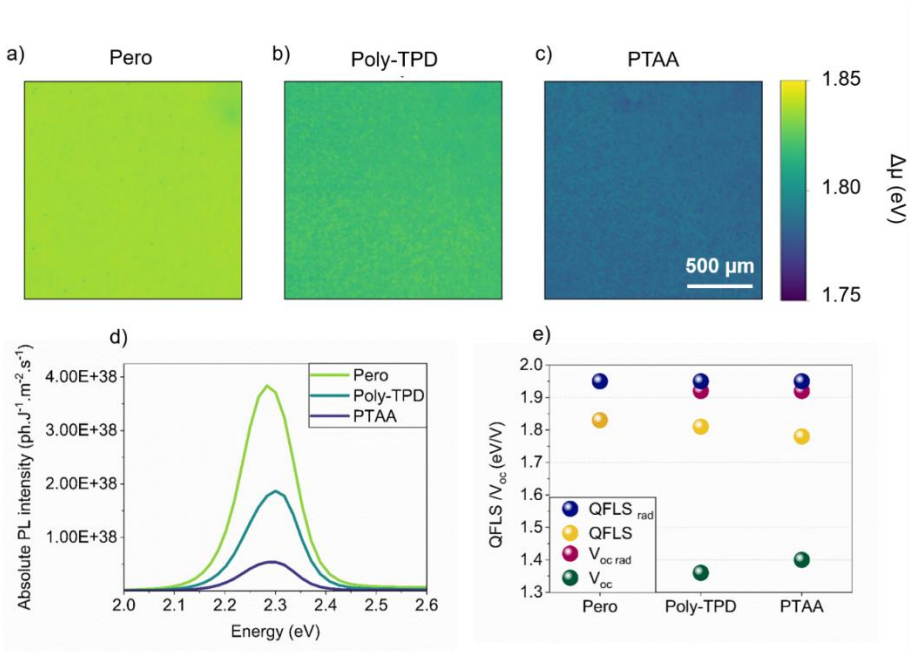

Figure 3. Photoluminescence Imaging Analysis. Hyperspectral measurements on the stacks ITO/SnO_2/KCl/$FAPbBr_3$ (pero), ITO/SnO_2/KCl/ $FAPbBr_3$/PTPD (PTPD) and ITO/SnO_2/KCl/ $FAPbBr_3$/PTAA (PTAA). quasi-Fermi level splitting (Δμ) maps for a) pero, b) PTPD and c) PTAA samples. d) Photoluminescence average spectra for the three maps e) QFLS values extracted from PL spectra compared with radiative QFLS $\Delta\mu_{rad}$, open circuit voltage V_{oc} and radiative open circuit voltage $V_{oc\ rad}$.

The stability of the unencapsulated solar cells, stored under ISOS-D-1 conditions (room temperature, ambient conditions), was evaluated, and shown in **Figure 4a**. It was observed that all devices exhibited a slight increase in performance during the first week after fabrication, followed by a stabilization of efficiency over a period of 1000 hours. To understand the adhesion between the HTL and ITO top electrode, we performed a bending test with a cylinder radius of 18 mm. Both PTAA and PTPD demonstrated stable performance in terms of adhesion to ITO, with both HTLs maintaining over 80% PCE even after 1200 bending cycles. PTPD surpassed the performance of the other HTLs by retaining 94% of its PCE after 1200 bending cycles.

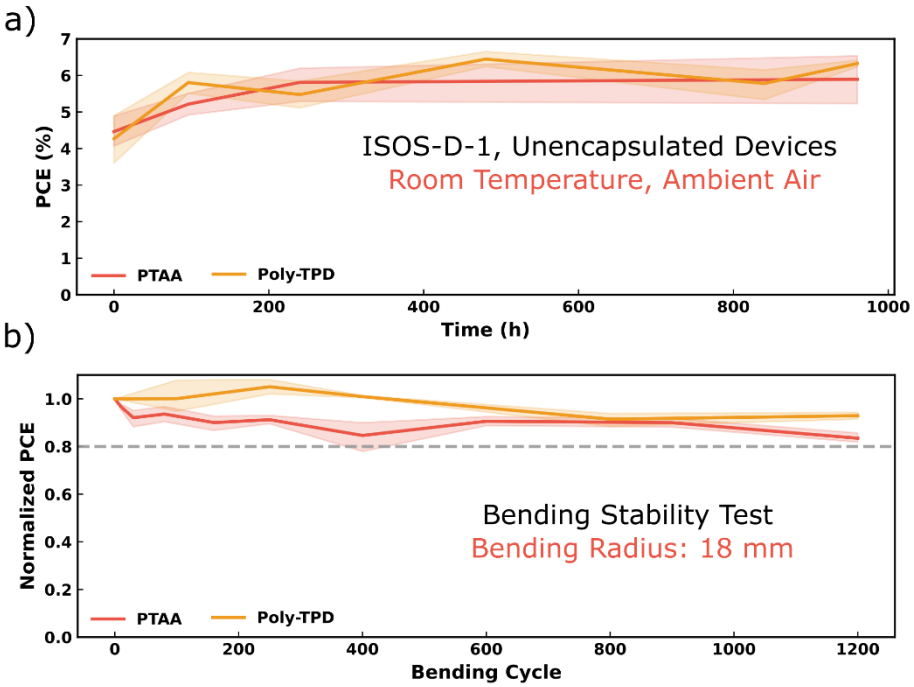

Figure 4. a. The stability measurement of solar cells with different HTLs under ISOS-1D conditions. b. The normalized PCE of devices going through the mechanical bending test.

The mini modules we fabricated consist of two cells with a total active area of 2.9 cm^2 with the PET/ITO/SnO_2/KCl/$FAPbBr_3$/PTAA/ITO device architecture. The high geometrical fill factor (GFF) of 97.83% is achieved by performing a P1-P2-P3 laser ablation with the width of 160 µm (**Figure S7**). The champion module achieved a PCE of 4.7%, with a voltage of 2.62 V, a current density of 4.97 mA/cm^2, and a fill factor (FF) of 71.45%. As far as our knowledge goes, this is the first flexible $FAPbBr_3$-based module reported. The current-voltage (IV) characteristics of the device are presented in **Figure 5a**.

We plotted the PCE and AVT of various flexible and rigid ST-PSCs reported in the literature (**Figure 5b**). Compared with the literature results, our device outperforms the existing flexible ST-SCs by a PCE of 6.7%, setting a record for flexible $FAPbBr_3$ ST-PSCs. The CIE chromaticity diagram (1931) is used to represent the CIE coordinates of the flexible ST-PSC device under AM1.5G (air mass 1.5 global) light conditions in **Figure 5c**. To provide readers with an understanding of the AVT of the fabricated cell (55%), we captured a photographic image comparing the view of the Roman Colosseum without any filtering and the view when the camera is filtered by a flexible ST-PSC shown in **Figure 5d**. This image serves as a visual representation of the transparency and color index of the flexible ST-PSC when applied to transparent surfaces such windows to form a tinted architectural glass.

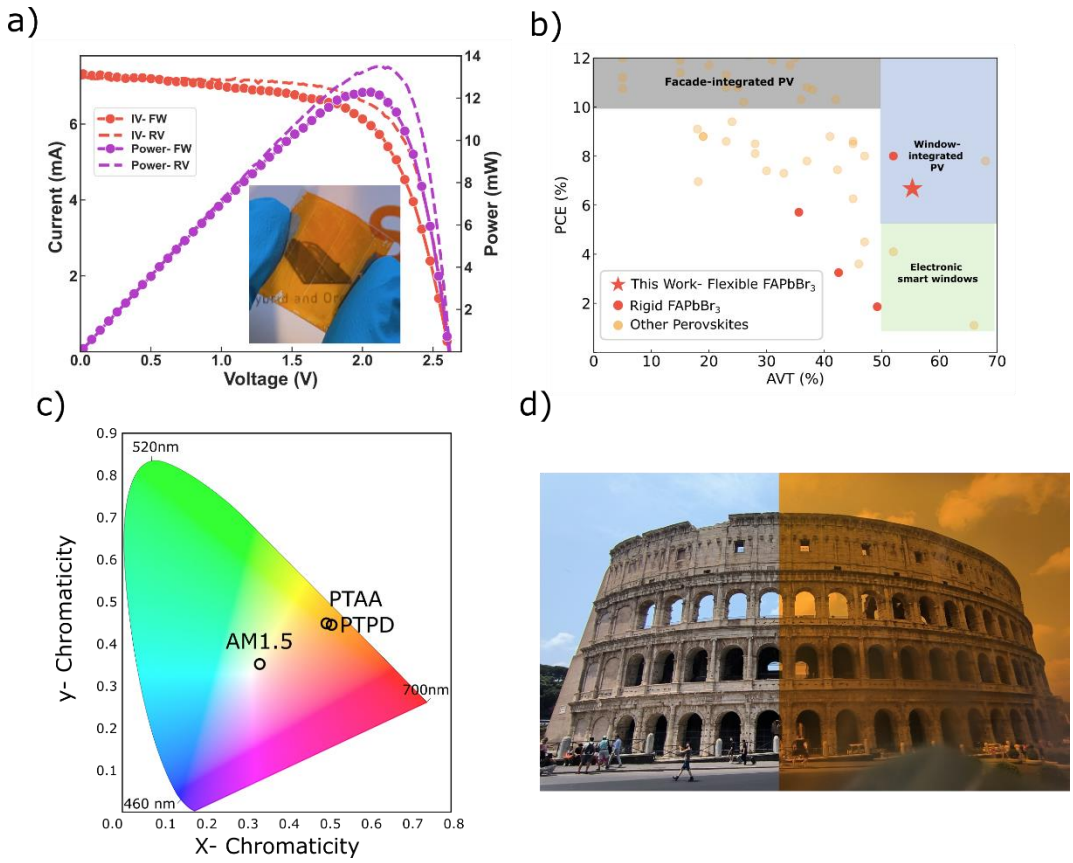

Figure 5. a. The current voltage and power curve of 2.9 cm^2 minimodule. b. PCE and AVT of flexible and rigid ST-PSCs along with their potential application areas. c. Photograph showing the view of Colosseum through the flexible ST-PSC. d. A schematic demonstrating possible application for the flexible ST-PSC as a detachable window-integrated PV. e. The CIE chromaticity diagram (1931) presenting color coordinates of the flexible ST-PSC under AM1.5G illumination.

In summary, we presented the fabrication and characterization of flexible and transparent perovskite solar cells with $FAPbBr_3$ absorber for the first time. We have demonstrated the positive effect of potassium treatment on the SnO2/$FAPbBr_3$ interface and investigated the effect of HTL on the performance, bifacility factor, and stability of devices. Best solar cells showed up to 55% AVT and a bifaciality factor approaching unity which results in similar performance from both sides. Record efficiencies of 6.8% under AM1.5 G conditions, and 18.7% PCE under indoor illumination is obtained for flexible $FAPbBr_3$-based perovskite. In addition, flexible $FAPbBr_3$-based minimodules fabricated for the first time achieving a PCE of 4.7% and a high geometrical fill factor up to 98%. We highlight the feasibility of the flex-ST-PSCs, demonstrating their transparency and taking advantage of the high bifacility factor up to 98%, allowing electric power generation from both side under sunlight and indoor lighting. The flexibility of cells makes them ideal for integrated transparent photovoltaic applications as an efficient and versatile energy solution.

Acknowledgments

This research has received funding from the European Union's Horizon 2020 research and innovation program under Grant Agreement No 101007084 (CITYSOLAR) and the European Union's Horizon 2020 Research and Innovation Program under grant agreement no. 763989 APOLO. This publication reflects only the authors' views, and the European Union is not liable for any use that may be made of the information contained therein. The financial support from the Lazio Region through ISIS@M- ACH (IR approved by Giunta Regionale no. G10795, 7 August 2019 published by BURL no. 69, 27 August 2019).

Supporting information

Methods, Hyperspectral PL imaging, Radiative Limit, PL Models, TPV and TPC measurements, Indoor JV curve of the champion cell, transmittance and reflectance of PSCs, optical loss analysis of PSCs, Optical microscopic of image of module interconnections, supplementary tables.

References

(1) Green, M. A.; Dunlop, E. D.; Siefer, G.; Yoshita, M.; Kopidakis, N.; Bothe, K.; Hao, X. Solar Cell Efficiency Tables (Version 61). *Prog. Photovolt.* **2023**, *31* (1), 3–16.
(2) Park, J.; Kim, J.; Yun, H.-S.; Paik, M. J.; Noh, E.; Mun, H. J.; Kim, M. G.; Shin, T. J.; Seok, S. I. Controlled Growth of Perovskite Layers with Volatile Alkylammonium Chlorides. *Nature* **2023**, *616* (7958), 724–730.
(3) Ma, Y.; Lu, Z.; Su, X.; Zou, G.; Zhao, Q. Recent Progress toward Commercialization of Flexible Perovskite Solar Cells: From Materials and Structures to Mechanical Stabilities. *Adv. Energy Sustain. Res.* **2023**, *4* (1), 2200133.
(4) Podapangi, S. K.; Jafarzadeh, F.; Mattiello, S.; Korukonda, T. B.; Singh, A.; Beverina, L.; Brown, T. M. Green Solvents, Materials, and Lead-Free Semiconductors for Sustainable Fabrication of Perovskite Solar Cells. *RSC Adv.* **2023**, *13* (27), 18165–18206.
(5) Gao, Y.; Huang, K.; Long, C.; Ding, Y.; Chang, J.; Zhang, D.; Etgar, L.; Liu, M.; Zhang, J.; Yang, J. Flexible Perovskite Solar Cells: From Materials and Device Architectures to Applications. *ACS Energy Lett.* **2022**, *7* (4), 1412–1445.
(6) Chen, Z.; Cheng, Q.; Chen, H.; Wu, Y.; Ding, J.; Wu, X.; Yang, H.; Liu, H.; Chen, W.; Tang, X.; Lu, X.; Li, Y.; Li, Y. Perovskite Grain-Boundary Manipulation Using Room-Temperature Dynamic Self-Healing "Ligaments" for Developing Highly Stable Flexible Perovskite Solar Cells with 23.8% Efficiency. *Adv. Mater.* **2023**, *35* (18), e2300513.
(7) Shi, B.; Duan, L.; Zhao, Y.; Luo, J.; Zhang, X. Semitransparent Perovskite Solar Cells: From Materials and Devices to Applications. *Adv. Mater.* **2020**, *32* (3), e1806474.
(8) Matteocci, F.; Rossi, D.; Castriotta, L. A.; Ory, D.; Mejaouri, S.; der Maur, M. A.; Sauvage, F.; Cacovich, S.; Di Carlo, A. Wide Bandgap Halide Perovskite Absorbers for Semi-Transparent Photovoltaics: From Theoretical Design to Modules. *Nano Energy* **2022**, *101* (107560), 107560.
(9) Bing, J.; Caro, L. G.; Talathi, H. P.; Chang, N. L.; Mckenzie, D. R.; Ho-Baillie, A. W. Y. Perovskite Solar Cells for Building Integrated Photovoltaics—Glazing Applications. *Joule* **2022**, *6* (7), 1446–1474.
(10) Li, Q.; Zheng, Y.; Guo, X.; Zhang, G.; Ding, G.; Shi, Y.; Li, F.; Sun, M.; Shao, Y. Interface Engineering Enhances the Photovoltaic Performance of Wide Bandgap $FAPbBr_3$ Perovskite for Application in Low-light Environments. *Adv. Funct. Mater.* **2023**. https://doi.org/10.1002/adfm.202303729.
(11) *Key Parameters and Thresholds Values for Obtaining High Performance Perovskite Solar Cells Indoors from Full Br Compositional and Bandgap Engineering*.

(12) Gan, S.; Sun, H.; Li, C.; Dou, D.; Li, L. Bifacial Perovskite Solar Cells: A Universal Component That Goes beyond Albedo Utilization. *Sci. Bull. (Beijing)* **2023**, *68* (19), 2247–2267.
(13) Yang, B.; Zhang, M.; Qiao, G.; Zhang, H. Perovskite Solar Cells: Emerging Photovoltaic Technology for Achieving Net-zero Emission Agrivoltaics Ecosystem. *Sol. RRL* **2023**. https://doi.org/10.1002/solr.202300217.
(14) Traverse, C. J.; Pandey, R.; Barr, M. C.; Lunt, R. R. Emergence of Highly Transparent Photovoltaics for Distributed Applications. *Nat. Energy* **2017**, *2* (11), 849–860.
(15) Thompson, E. P.; Bombelli, E. L.; Shubham, S.; Watson, H.; Everard, A.; D'Ardes, V.; Schievano, A.; Bocchi, S.; Zand, N.; Howe, C. J.; Bombelli, P. Tinted Semi-transparent Solar Panels Allow Concurrent Production of Crops and Electricity on the Same Cropland. *Adv. Energy Mater.* **2020**, *10* (35), 2001189.
(16) Yang, C.; Liu, D.; Bates, M.; Barr, M. C.; Lunt, R. R. How to Accurately Report Transparent Solar Cells. *Joule* **2019**, *3* (8), 1803–1809.
(17) Lunt, R. R. Theoretical Limits for Visibly Transparent Photovoltaics. *Appl. Phys. Lett.* **2012**, *101* (4), 043902.
(18) Barichello, J.; Di Girolamo, D.; Nonni, E.; Paci, B.; Generosi, A.; Kim, M.; Levtchenko, A.; Cacovich, S.; Di Carlo, A.; Matteocci, F. Semi-transparent Blade-coated $FAPbBr_3$ Perovskite Solar Cells: A Scalable Low-temperature Manufacturing Process under Ambient Condition. *Sol. RRL* **2023**, *7* (3), 2200739.
(19) Yue, W.; Yang, H.; Cai, H.; Xiong, Y.; Zhou, T.; Liu, Y.; Zhao, J.; Huang, F.; Cheng, Y.-B.; Zhong, J. Printable High-Efficiency and Stable FAPbBr3 Perovskite Solar Cells for Multifunctional Building-Integrated Photovoltaics. *Adv. Mater.* **2023**, e2301548.
(20) Zhu, H.; Wu, W.; Wu, Y.; Zhang, D.; Zhan, H.; Cheng, Y.; Wang, L.; Qin, C. Δ-phase Management of $FAPbBr_3$ for Semitransparent Solar Cells. *Adv. Opt. Mater.* **2023**, 2202827.
(21) Liu, Y.; Kim, B. J.; Wu, H.; Boschloo, G.; Johansson, E. M. J. Efficient and Stable FAPbBr3 Perovskite Solar Cells via Interface Modification by a Low-Dimensional Perovskite Layer. *ACS Appl. Energy Mater.* **2021**, *4* (9), 9276–9282.
(22) Zhang, Y.; Liang, Y.; Wang, Y.; Guo, F.; Sun, L.; Xu, D. Planar FAPbBr3 Solar Cells with Power Conversion Efficiency above 10%. *ACS Energy Lett.* **2018**, *3* (8), 1808–1814.
(23) Matteocci, F.; Girolamo, D. D.; Vidon, G.; Barichello, J.; Giacomo, F. D.; Jafarzadeh, F.; Paci, B.; Generosi, A.; Kim, M.; Castriotta, L. A.; Frégnaux, M.; Guillemoles, J.-F.; Schulz, P.; Ory, D.; Cacovich, S.; Carlo, A. D. Breaking 1.7V Open Circuit Voltage in Large Area Transparent Perovskite Solar Cells Using Bulk and Interfaces Passivation. *Research Square*, 2023. https://doi.org/10.21203/rs.3.rs-3139318/v1.
(24) Liu, Y.; Kim, B. J.; Wu, H.; Yuan, L.; Zhu, H.; Liu, A.; Johansson, E. M. J. Flexible Lead Bromide Perovskite Solar Cells. *ACS Appl. Energy Mater.* **2020**, *3* (10), 9817–9823.
(25) Park, S. Y.; Zhu, K. Advances in SnO2 for Efficient and Stable N-i-p Perovskite Solar Cells. *Adv. Mater.* **2022**, *34* (27), e2110438.
(26) *Simultaneous Contact and Grain-Boundary Passivation in Planar Perovskite Solar Cells Using SnO2-KCl Composite Electron Transport Layer*.
(27) Liu, X.; Zhang, Y.; Shi, L.; Liu, Z.; Huang, J.; Yun, J. S.; Zeng, Y.; Pu, A.; Sun, K.; Hameiri, Z.; Stride, J. A.; Seidel, J.; Green, M. A.; Hao, X. Exploring Inorganic Binary Alkaline Halide to Passivate Defects in Low-temperature-processed Planar-structure Hybrid Perovskite Solar Cells. *Adv. Energy Mater.* **2018**, *8* (20), 1800138.
(28) Bu, T.; Li, J.; Zheng, F.; Chen, W.; Wen, X.; Ku, Z.; Peng, Y.; Zhong, J.; Cheng, Y.-B.; Huang, F. Universal Passivation Strategy to Slot-Die Printed SnO2 for Hysteresis-Free Efficient Flexible Perovskite Solar Module. *Nat. Commun.* **2018**, *9* (1), 4609.

(29) Hidayat, R.; Nurunnizar, A. A.; Fariz, A.; Herman; Rosa, E. S.; Shobih; Oizumi, T.; Fujii, A.; Ozaki, M. Revealing the Charge Carrier Kinetics in Perovskite Solar Cells Affected by Mesoscopic Structures and Defect States from Simple Transient Photovoltage Measurements. *Sci. Rep.* **2020**, *10* (1), 19197.
(30) Jiménez-López, J.; Cambarau, W.; Cabau, L.; Palomares, E. Charge Injection, Carriers Recombination and HOMO Energy Level Relationship in Perovskite Solar Cells. *Sci. Rep.* **2017**, *7* (1), 6101.
(31) Xu, C.; Zhang, S.; Fan, W.; Cheng, F.; Sun, H.; Kang, Z.; Zhang, Y. Pushing the Limit of Open-Circuit Voltage Deficit via Modifying Buried Interface in CsPbI3 Perovskite Solar Cells. *Adv. Mater.* **2023**, *35* (7), e2207172.
(32) Wu, J.; Cha, H.; Du, T.; Dong, Y.; Xu, W.; Lin, C.-T.; Durrant, J. R. A Comparison of Charge Carrier Dynamics in Organic and Perovskite Solar Cells. *Adv. Mater.* **2022**, *34* (2), e2101833.
(33) *Tailored Phase Conversion under Conjugated Polymer Enables Thermally Stable Perovskite Solar Cells with Efficiency Exceeding 21%*.
(34) Mozaffari, N.; Walter, D.; White, T. P.; Bui, A. D.; Tabi, G. D.; Weber, K.; Catchpole, K. R. Unraveling the Role of Energy Band Alignment and Mobile Ions on Interfacial Recombination in Perovskite Solar Cells. *Sol. RRL* **2022**, *6* (6), 2101087.
(35) Chen, P.; Bai, Y.; Wang, L. Minimizing Voltage Losses in Perovskite Solar Cells. *Small Struct.* **2021**, *2* (1), 2000050.
(36) Jiang, Q.; Song, Z.; Bramante, R. C.; Ndione, P. F.; Tirawat, R.; Berry, J. J.; Yan, Y.; Zhu, K. Highly Efficient Bifacial Single-Junction Perovskite Solar Cells. *Joule* **2023**, *7* (7), 1543–1555.
(37) Giuliano, G.; Bonasera, A.; Arrabito, G.; Pignataro, B. Semitransparent Perovskite Solar Cells for Building Integration and Tandem Photovoltaics: Design Strategies and Challenges. *Sol. RRL* **2021**, *5* (12), 2100702.
(38) Reddy, S. H.; Di Giacomo, F.; Matteocci, F.; Castriotta, L. A.; Di Carlo, A. Holistic Approach toward a Damage-Less Sputtered Indium Tin Oxide Barrier Layer for High-Stability Inverted Perovskite Solar Cells and Modules. *ACS Appl. Mater. Interfaces* **2022**, *14* (45), 51438–51448.
(39) Wang, K.-L.; Zhou, Y.-H.; Lou, Y.-H.; Wang, Z.-K. Perovskite Indoor Photovoltaics: Opportunity and Challenges. *Chem. Sci.* **2021**, *12* (36), 11936–11954.
(40) Wojciechowski, K.; Forgács, D. Commercial Applications of Indoor Photovoltaics Based on Flexible Perovskite Solar Cells. *ACS Energy Lett.* **2022**, *7* (10), 3729–3733.
(41) Skafi, Z.; Xu, J.; Mottaghitalab, V.; Mivehi, L.; Taheri, B.; Jafarzadeh, F.; Podapangi, S. K.; Altamura, D.; Guascito, M. R.; Barba, L.; Giannini, C.; Rizzo, A.; De Rossi, F.; Javanbakht Lomeri, H.; Sorbello, L.; Matteocci, F.; Brunetti, F.; Brown, T. M. Highly Efficient Flexible Perovskite Solar Cells on Polyethylene Terephthalate Films via Dual Halide and Low-dimensional Interface Engineering for Indoor Photovoltaics. *Sol. RRL* **2023**. https://doi.org/10.1002/solr.202300324.
(42) Cacovich, S.; Vidon, G.; Degani, M.; Legrand, M.; Gouda, L.; Puel, J.-B.; Vaynzof, Y.; Guillemoles, J.-F.; Ory, D.; Grancini, G. Imaging and Quantifying Non-Radiative Losses at 23% Efficient Inverted Perovskite Solar Cells Interfaces. *Nat. Commun.* **2022**, *13* (1), 2868.
(43) Stolterfoht, M.; Wolff, C. M.; Márquez, J. A.; Zhang, S.; Hages, C. J.; Rothhardt, D.; Albrecht, S.; Burn, P. L.; Meredith, P.; Unold, T.; Neher, D. Visualization and Suppression of Interfacial Recombination for High-Efficiency Large-Area Pin Perovskite Solar Cells. *Nat. Energy* **2018**, *3* (10), 847–854.
(44) Milotti, V.; Cacovich, S.; Ceratti, D. R.; Ory, D.; Barichello, J.; Matteocci, F.; Di Carlo, A.; Sheverdyaeva, P. M.; Schulz, P.; Moras, P. Degradation and Self-healing of $FAPbBr_3$ Perovskite under Soft-X-ray Irradiation. *Small Methods* **2023**, *7* (9). https://doi.org/10.1002/smtd.202300222.
(45) Caprioglio, P.; Stolterfoht, M.; Wolff, C. M.; Unold, T.; Rech, B.; Albrecht, S.; Neher, D. On the Relation between the Open-circuit Voltage and Quasi-Fermi Level Splitting in Efficient Perovskite Solar Cells. *Adv. Energy Mater.* **2019**, *9* (33). https://doi.org/10.1002/aenm.201901631.

Supporting Information

Methods

Materials

Formamidinium bromide (FABr, ≥ 99.99%), iso-Pentylammonium chloride, and neo-Pentylammonium chloride were purchased from Greatcell Solar Materials. Lead(II) bromide (PbBr2) for the perovskite precursor (99.99%) was purchased from Tokyo Chemical Industry (TCI). Poly[bis(4-phenyl)(2,4,6-trimethylphenyl) amine] (PTAA, 10 kDa) and Poly[N,N'-bis(4-butylphenyl)-N,N'-bisphenylbenzidine] (PTPD, 10 – 30 kDa) were purchased from Solaris Chem. Tin(IV) oxide (SnO2) colloidal nanoparticles in water (15% wt) were purchased from Alpha-Aesar, Dimethyl sulfoxide (DMSO, ≥ 99.99%), potassium chloride (KCl, 99.0%), toluene (99.5%), tert-butylpyridine (TBP, 96%), Li bis(trifuoromethanesulfonyl)imide (99.95%), acetonitrile (99.8%), and 2-propanol (99.5%) were purchased from Sigma- Aldrich.

Device Fabrication

PET/ITO substrates were etched by laser (model) and cut in 2.5×2.5 cm^2 substrate sizes. The substrates were washed in ultrasonic bath using detergent, water, and 2-propanol and then treated under UV-Ozone for 15 minutes. SnO2 nanoparticles (15 %wt) where spin coated with the speed of 6000 rpm for 35 s and then annealed at 100 °C for 60 minutes. For the potassium treated samples, 50 mM aqueous solution of KCl were spin coated at 3000 rpm for 30 s followed by annealing at 100 °C for 15 minutes. Substrates UV-Ozone treated right before the perovskite deposition and a 1.4 M solution of FAPbBr3 in DMSO is deposited at 4000 rpm, 20s followed by anti-solvent dripping of ethyl-acetate at the 10^{th} second. The substrates annealed at 80 °C for 10 minutes. neo-Pentylammonium chloride and iso-Pentylammonium chloride (1 mg of each) were dissolved in 1 ml of Isopropyl alcohol and spin coated on the perovskite layer to passivate defects as reported in our previous work[23]. For PTAA and PTPD, 10 mg/ml solution in toluene containing 10 µL/ml TPB and 5 µL/ml Li-TFSI salt (170 mg/ml in acetonitrile) was deposited at 4000 rpm for 20 s. Finally, 150 nm of ITO was sputtered on top using power using an industrial in-line magnetron sputtering (KENOSISTEC S.R.L., KS 400 In-Line) with the same procedure to our previous study[18].For modules, P1, P2 and P3 etching processes have been performed by using a raster scanning laser (Wophotonics, Yb:KGW, λ = 355 nm, 5 ps, pulsed at 2000 kHz with a fluence per pulse for patterning cells and for P1, P2 and P3 of 34.33, 18.06 and 16.68 mJ cm-2, respectively). P2 is performed by placing 6 lines beside different fluences of ~1 mJ cm-2 difference, with an average fluence per pulse of 18.06 mJ cm-2. The module layout is composed by a 25 × 25 mm^2 substrate size, formed by 2 series connected cells with 7.38 mm × 19.65 mm cell width and height, P1-P2-P3 interconnection of 160 µm, 2.9cm^2 active area and 97.83% geometrical fill factor.

Characterizations

All solar cells were measured under standard AM1.5 conditions using a class A solar simulator (ABET Sun 2000) with an aperture area of 0.3 cm^2. A Si reference cell (RR226-O, RERA Solutions) was used for calibration of the sun simulator. The external quantum efficiency (EQE) spectra, transient photovoltage

(TPV), and transient photocurrent (TPC), were measured using a measurement system from Arkeo–Cicci research s.r.l. The scanning electron micros- copy images were captured using a TESCAN MIRA microscope. A Rigaku SmartLab SE was used to measure X-ray diffraction patterns. Olympus Lext OLS 3100 is used to obtain optical microscopy images.

Hyperspectral PL imaging

A home-made microscope was employed for imaging samples. The illumination source consisted of a 405nm LED from Thorlabs, which was directed onto the sample and filtered through a 424nm short-pass filter (Semrock FF01-424/SP-25). A dichroic mirror (Thorlabs DMLP425) was utilized to eliminate both the excitation light and the photoluminescence, followed by a 430nm long-pass filter (SemRock FF01-430/LP-25). The collected light was directed to a hyperspectral imager from Photon etc., and subsequently to a CCD camera. All measurements were conducted in air atmosphere.

The acquired data underwent a calibration procedure, as detailed in previous work[44], along with a rectification of the data cubes. A custom software was developed for extracting the quasi-Fermi Level Splitting from the acquired data, utilizing the generalized Planck's law of radiation. A Gaussian filter was applied to the QFLS maps.

Radiative limit

The QFLS in the radiative limit ($QFLS^{rad}$) is defined as:

$$QFLS^{rad} = \frac{kT}{q} \cdot \ln\left(\frac{I_{ph}}{q\phi_{em}}\right)$$

where I_ph is the photocurrent due to the considered illumination and ϕ_em is the PL emission of the absorber in thermal equilibrium with its surrounding at 300 K and kT the thermal energy of the charge carriers.

In our analysis, we consider the photocurrent generated by a monochromatic radiation at 405 nm with a 1 sun-equivalent power density to match the experimental conditions used in the steady measurements and directly compare the $QFLS^{rad}$ with the QFLS experimentally measured on bare absorbers and stacks. The PL emission ϕ_em corresponds to ϕ_em=∫α(E) ϕ_BB^300K (E)dE, where ϕ_BB^300K is the blackbody radiation at 300K and a(E) is the absorbance of the perovskite.

The radiative V_{oc} (V_{oc}^{rad}) was calculated from :

$$V_{oc}^{rad} = \frac{kT}{q} \cdot \ln\left(\frac{J_{sc}}{J_{0rad}}\right)$$

Where

J_{0rad}=q∫EQEϕ_BB^300K (E)dE

PL models

The absolute photoluminescence data were fitted with the generalized Planck's law by:

$$I_{PL}(E) = \frac{\frac{2\pi}{h^3c^2}E^2 a(E)}{\exp\left(\frac{E-\Delta\mu}{kT}\right)}$$

Where h is the Planck's constant, c the speed of light, E the photon energy, a(E) the absorptivity of the sample taking into account sub-band gap absorption, Δμ the QFLS, and kT the thermal energy of the charge carriers.

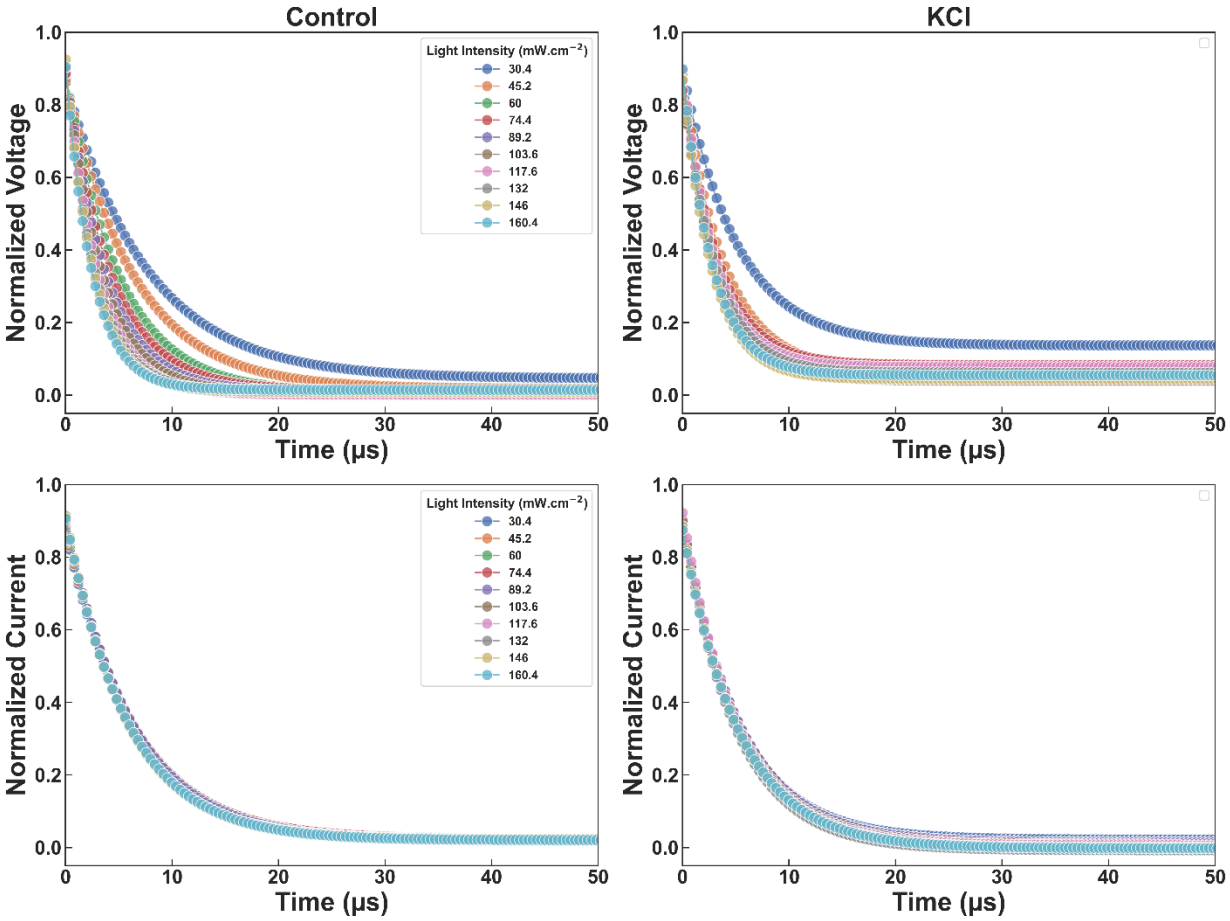

Figure S1. TPV (up) and TPC (down) measurements for champion control and KCl devices under an LED light with intensity varying from 30.4 to 160.4 mW.cm^{-2}.

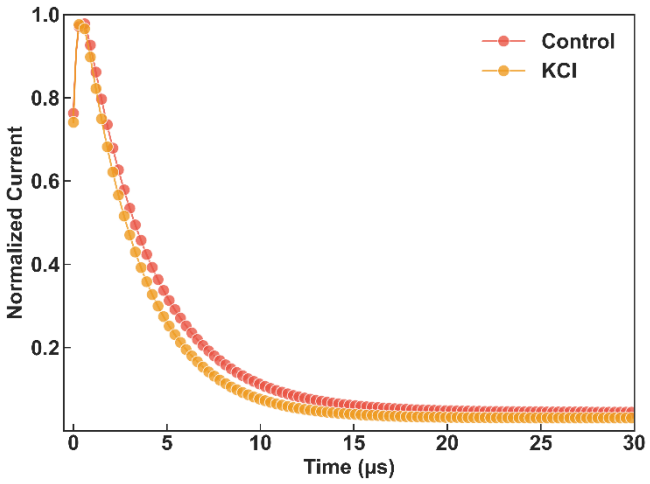

Figure S2- Normalized Transient photocurrent measurement under LED light with power density of 100 mW.cm^{-2}.

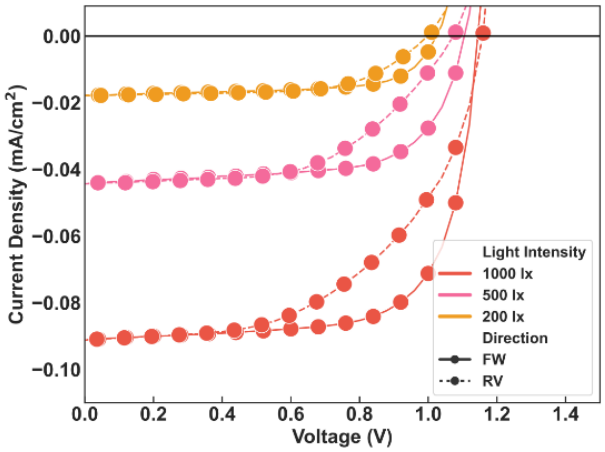

Figure S3. JV curves of champion cell with PTAA as HTL under indoor light conditions (200 lx, 500 lx, and 1000 lx).

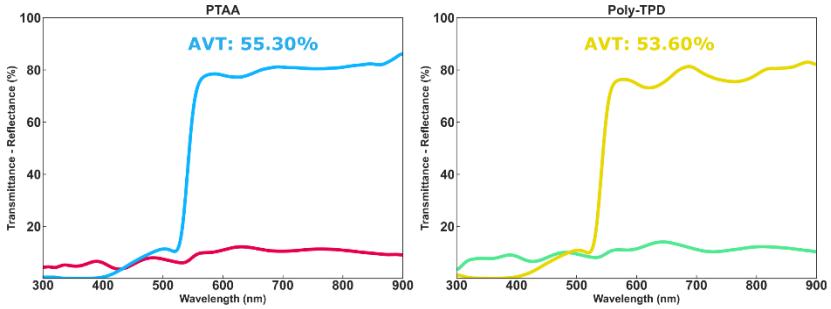

Figure S4. Transmittance and reflectance of flexible ST-PSCs using PTAA and PTPD as HTL.

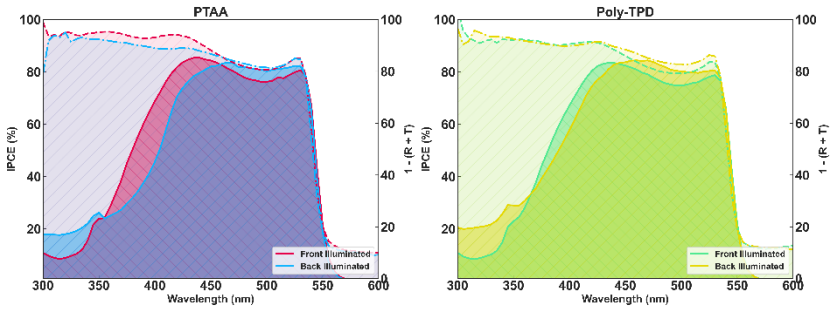

Figure S5. The IPCE of flex-ST-PSCs versus 1 – (R + T) when illuminated from front and back.

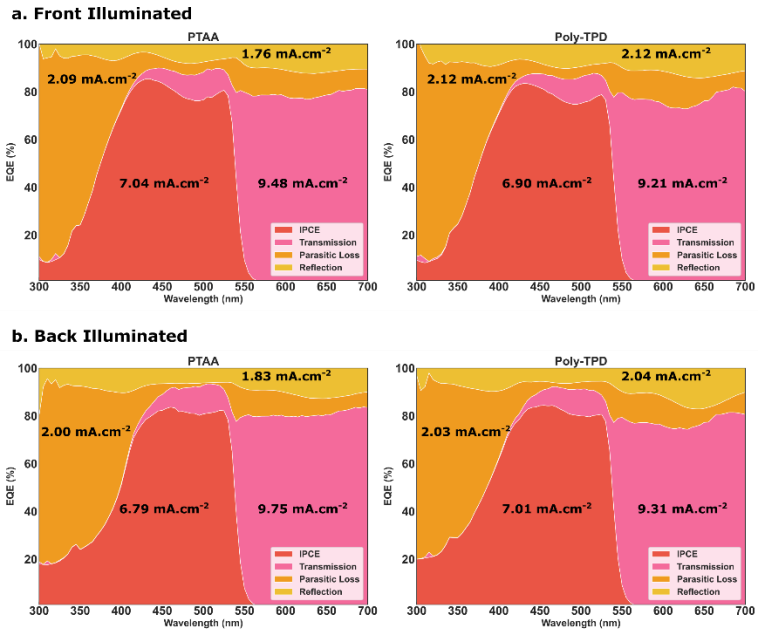

Figure S6. Optical loss analysis of flex-ST-PSCs fabricated with different HTLs illuminated from (a) front and (b).

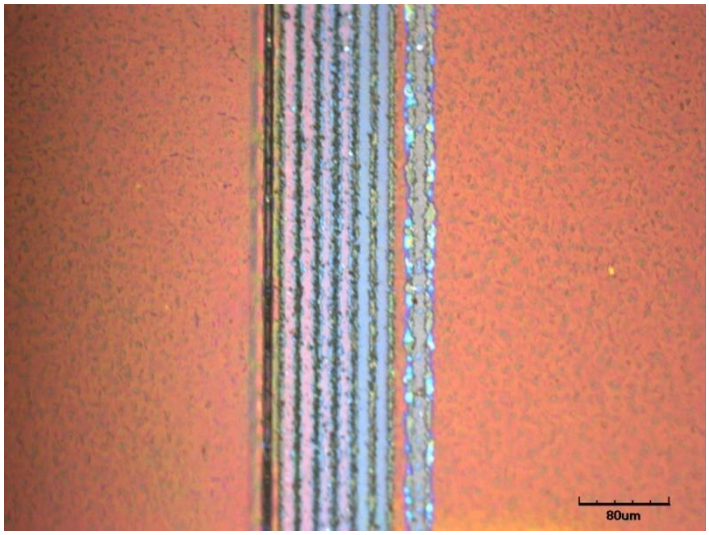

Figure S7. The optical microscopic image of the P1-P2-P3 interconnections of the mini-module.

Table S1. TPC lifetimes obtained from **Figure 2 c**.

Sample	τ_1 (µs)	τ_2(µs)
Control	8.42	8.23
KCl	3.06	0.22

Table S2. The photovoltaic parameters, light utilization, and efficiency of champion devices utilizing PTAA and PTPD as hole transport material (HTL) under AM 1.5G condition.

HTL	Illuminated Side	V_{OC} (V)	J_{SC} (mA.cm^{-2})	FF (%)	PCE (%)	AVT (%)	LUE (%)
PTAA	Front	1.40	7.4	65.7	6.8	55.3	3.74
	Back	1.37	6.9	65.5	6.2		
PTPD	Front	1.36	7.2	68.4	6.7	53.6	3.60
	Back	1.34	6.9	67.6	6.2		

Table S3. The photovoltaic parameters, light utilization, and efficiency of champion devices utilizing PTAA and PTPD as HTL under indoor conditions (1000 lx).

HTL	Illuminated Side	V_{OC} (V)	J_{SC} (mA.cm^{-2})	Integrated J_{SC} (mA.cm^{-2})	FF (%)	PCE (%)	LUE (%)
PTAA	Front	1.16	0.093	0.094	68.2	18.8	10.34
	Back	1.15	0.093	0.087	65.1	17.8	
PTPD	Front	1.10	0.092	0.092	68.8	17.9	8.75
	Back	1.16	0.095	0.091	61.1	17.0	

Table S4. AVT, CRI, and Color coordinates of flex ST-PSCs with different HTLs with 1.4 M $FAPbBr_3$.

HTL	AVT (%)	CRI	CIEL*a*b Coordinates

			L*	a*	b*
PTAA	55.3	45.03	78.4	22.6	80.3
PTPD	53.60	45.08	77.4	21.5	80.4

Table S5. Radiative V_{OC} and V_{OC} of full stack cells and Urbach, QFLS, and radiative QFLS for half-stack (PET/ITO/SnO2/KCl/FAPbBr3/ISO-NEO/HTL).

HTL	V_{OC} rad (eV)	V_{OC} (eV)	Urbach (meV)	QFLSrad (eV)	QFLS (eV)
PTAA	1.92	1.40	17.53	1.95	1.78
PTPD	1.92	1.36	17.09	1.95	1.81